Article

Developmental Cell

Diacylglycerol Guides the Hopping of Clathrin-Coated Pits along Microtubules for Exo-Endocytosis Coupling

Graphical Abstract

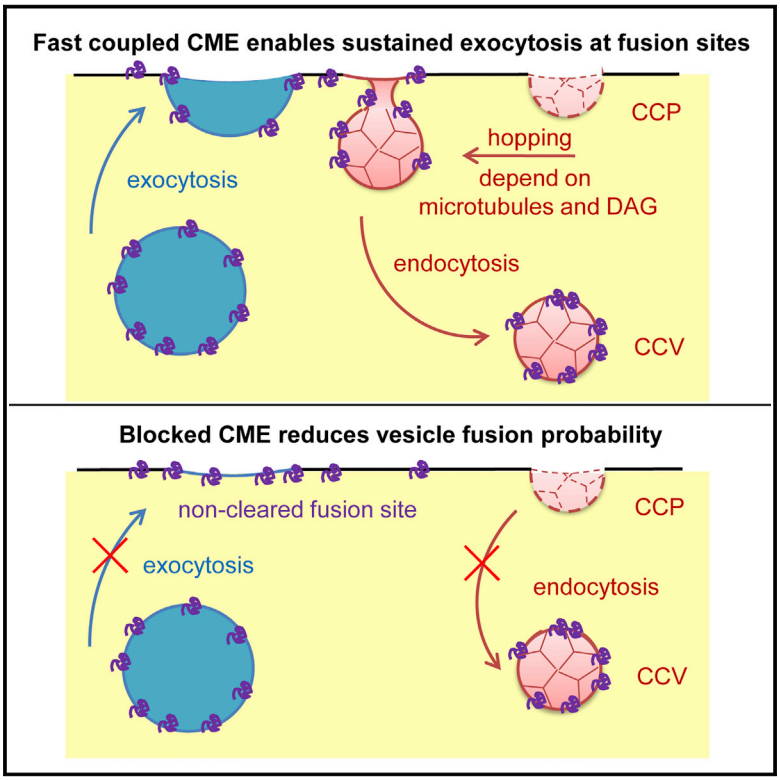

Highlights

- Pre-formed CCPs hop to nascent fusion sites to couple endocytosis with exocytosis
- Cortical microtubules anchored on the plasma membrane provide tracks for CCP hopping
- Local, transient diacylglycerol gradients guide the direction of CCP hopping
- Coupled endocytosis mediates rapid clearance of fusion sites for sustained exocytosis

Authors

Tianyi Yuan, Lin Liu, Yongdeng Zhang, ..., Jean Salamero, Yanmei Liu, Liangyi Chen

Correspondence

yanmeiliu@pku.edu.cn (Y.L.), lychen@pku.edu.cn (L.C.)

In Brief

Yuan et al. demonstrate that pre-formed clathrin-coated pits move to vesicle fusion sites along tracks provided by cortical microtubules, guided by local diacylglycerol concentration. This coupling mechanism mediates fast recycling of both plasma membrane and vesicular proteins, and it is required for the sustained exocytosis during repetitive stimulations.

Yuan et al., 2015, Developmental Cell *35*, 120–130
October 12, 2015
http://dx.doi.org/10.1016/j.devcel.2015.09.004

CellPress

CellPress

Developmental Cell
Article

Diacylglycerol Guides the Hopping of Clathrin-Coated Pits along Microtubules for Exo-Endocytosis Coupling

Tianyi Yuan,[1,2,7] Lin Liu,[1,2,7] Yongdeng Zhang,[3,7] Lisi Wei,[1,2,7] Shiqun Zhao,[1,2] Xiaolu Zheng,[1,2] Xiaoshuai Huang,[1,2] Jerome Boulanger,[4] Charles Gueudry,[5,6] Jingze Lu,[3] Lihan Xie,[1,2] Wen Du,[3] Weijian Zong,[1,2] Lu Yang,[1,2] Jean Salamero,[4,5] Yanmei Liu,[1,2,*] and Liangyi Chen[1,2,*]

[1]State Key Laboratory of Membrane Biology, Beijing Key Laboratory of Cardiometabolic Molecular Medicine, Institute of Molecular Medicine, Peking University, Beijing 100871, China
[2]National Center for Nanoscience and Technology, Beijing 100871, China
[3]National Key Laboratory of Biomacromolecules, Institute of Biophysics, Chinese Academy of Sciences, Beijing 100101, China
[4]UMR144 CNRS/UPMC, Institut Curie, 75005 Paris, France
[5]PICT Cell and Tissue Imaging Core Facility, Institut Curie, 75005 Paris, France
[6]Roper Scientific SAS, 91017 Evry, France
[7]Co-first author
*Correspondence: yanmeiliu@pku.edu.cn (Y.L.), lychen@pku.edu.cn (L.C.)
http://dx.doi.org/10.1016/j.devcel.2015.09.004

SUMMARY

Many receptor-mediated endocytic processes are mediated by constitutive budding of clathrin-coated pits (CCPs) at spatially randomized sites before slowly pinching off from the plasma membrane (60–100 s). In contrast, clathrin-mediated endocytosis (CME) coupled with regulated exocytosis in excitable cells occurs at peri-exocytic sites shortly after vesicle fusion (~10 s). The molecular mechanism underlying this spatiotemporal coupling remains elusive. We show that coupled endocytosis makes use of pre-formed CCPs, which hop to nascent fusion sites nearby following vesicle exocytosis. A dynamic cortical microtubular network, anchored at the cell surface by the cytoplasmic linker-associated protein on microtubules and the LL5β/ELKS complex on the plasma membrane, provides the track for CCP hopping. Local diacylglycerol gradients generated upon exocytosis guide the direction of hopping. Overall, the CCP-cytoskeleton-lipid interaction demonstrated here mediates exocytosis-coupled fast recycling of both plasma membrane and vesicular proteins, and it is required for the sustained exocytosis during repetitive stimulations.

INTRODUCTION

Clathrin-mediated endocytosis (CME) mediates constitutive, receptor-mediated endocytosis in all eukaryotic cells. In neuron and endocrine cells, rapid release of neurotransmitters and hormones is accompanied by massive addition of newly fused vesicle membrane to the plasma membrane. Subsequently, coupled endocytosis rapidly initiates to clear the plasma membrane for the next round of fusion (Neher, 2010) and maintain the balance of cell surface membrane (Haucke et al., 2011).

CME initiates with the budding of clathrin-coated pits (CCPs) that recruit numerous proteins, which bend surface membrane, interact with specific cargo proteins, facilitate clathrin coat assembly, and mediate final membrane scission (McMahon and Boucrot, 2011). In non-excitable cells, CCPs constitutively bud at spatially random sites before slowly pinching off from the plasma membrane with cargo proteins to be retrieved (60–100 s) (Ehrlich et al., 2004; Loerke et al., 2009). In neuron and endocrine cells, membrane depolarization evokes massive exocytosis followed by coupled fast CME (time constants, 3–10 s) (Artalejo et al., 2002; He et al., 2008; Jockusch et al., 2005; Wu et al., 2009; Zhu et al., 2009). Moreover, regulated CME occurs mostly at the spatially confined peri-active zone after stimulation in neurons (Marie et al., 2004; Roos and Kelly, 1999; Wahl et al., 2013). How the slow, spatially randomized CME is synchronized to regulated exocytosis in time and space in excitable cells remains enigmatic.

Using dual-color total internal reflection fluorescence (TIRF) microscopy to monitor discrete exocytic and endocytic events simultaneously, here we visualize elementary exocytosis-coupled CME in insulin-secreting INS-1 cells. In addition to direct hits of exocytosis onto sites close to pre-formed CCPs or de novo formation of CCPs at fusion sites after exocytosis, we reveal an unexpected hopping of pre-formed CCPs to nearby nascent fusion sites. These hopping CCPs move on the plasma membrane, with cargo proteins such as Syt VII, to fusion sites before endocytosis. Cortical microtubules underneath the plasma membrane provide tracks for the hopping of CCPs, and transient diacylglycerol (DAG) gradients at fusion sites convey the spatial orientation of the movement. Overall, we present a concept that lateral hopping of CCPs with directionality precisely couples CME with exocytosis in space and time. In conjunction with membrane-cytoskeleton interaction and DAG gradient, hopping of CCPs may represent an efficient method to actively recycle vesicular components and clear fusion sites in excitable cells.

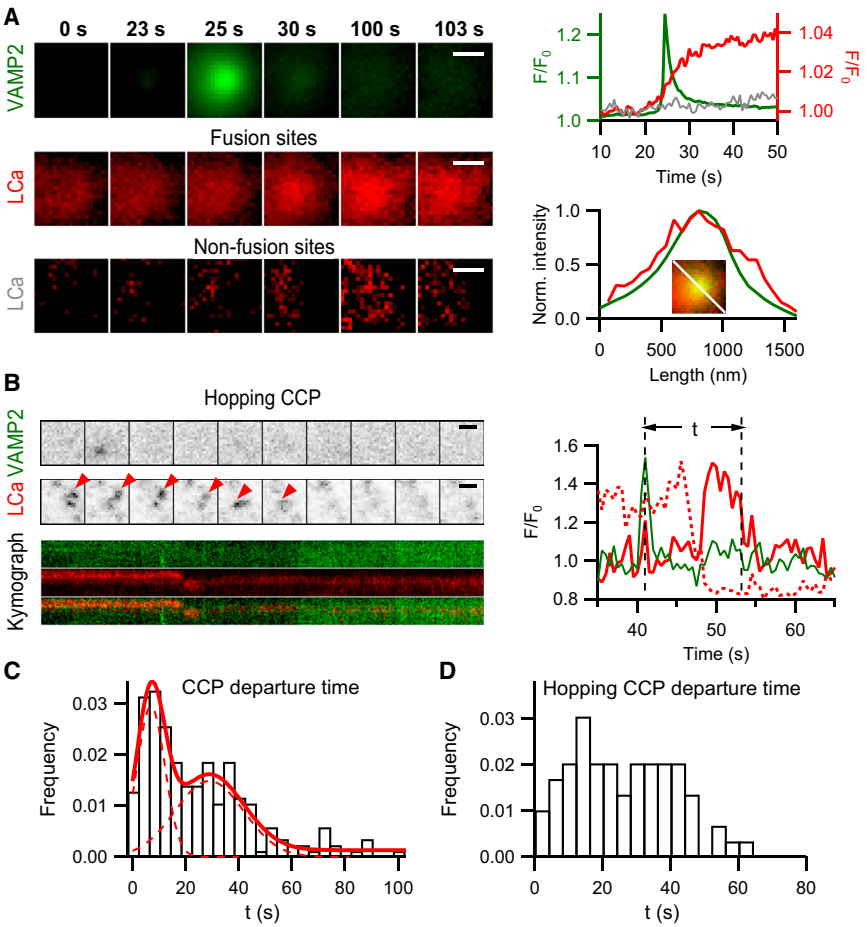

Figure 1. Pre-formed LCa Puncta Hop toward Nascent Fusion Sites for the Exo-Endocytosis Coupling

(A) Spatiotemporal association of clathrin with exocytosis in INS-1 cells co-transfected with VAMP2-pHluorin and LCa-DsRed. (Left) Time-lapse images show the average VAMP2-pHluorin signal (467 fusion events) at fusion sites (top) and the corresponding average LCa signal at fusion sites (middle) and at random sites (n = 467, bottom). (Right) Time courses of normalized fluorescence signals from average images on the left (top) and spatial profiles of the average VAMP2-pHluorin and LCa signals at fusion sites (bottom). Inset is the overlaid image.

(B) An example of a hopping CCP (arrowheads, see also Movie S1). (Left) Time-lapse images show VAMP2-pHluorin (top) and LCa signal (middle) at a fusion site, at 3-s intervals. Kymographs (bottom) are 150 s and 1.3 μm high. (Right) Time courses show normalized VAMP2-pHluorin (green) and LCa (red) signals at the fusion site. The dotted line represents the time course of normalized LCa signal at the original site before hopping, and departure time (t) represents the latency of a CCP departure after a fusion event.

(C) Normalized histogram of all exocytosis-coupled CCP departure times at fusion sites is shown (n = 215).

(D) Normalized histogram of departure times of hopping CCPs at fusion sites (n = 74) is shown. Scale bars, 500 nm. See also Figure S1 for other types of CCP recruitments at fusion sites and hopping CCP dynamics analysis and Figure S2 for coupled recruitment of Dyn1 at fusion sites.

RESULTS

The Elementary Coupling between CME and Exocytosis

We labeled VAMP2 with the fluorophore pHluorin, which remains quenched by acidic luminal pH until a vesicle fuses. At a cell footprint, a sudden focal brightening indicates a fusion pore opening; and the ensuing circular spread of the pHluorin signal signifies VAMP2 proteins diffusing away from the fusion site (Figure S1A; Allersma et al., 2004). To simultaneously detect endocytosis, we tagged the light chain of clathrin (LCa) with DsRed (Ehrlich et al., 2004; Merrifield et al., 2002), so that the budding off of a CCP could be recorded as the sudden disappearance of an LCa punctum (Figures S1A and S1B; Ehrlich et al., 2004; Loerke et al., 2009; Merrifield et al., 2005). Stimulation with high glucose and high potassium evoked massive exocytosis and the disappearance of LCa puncta over the entire cell footprint. Visual examination of individual VAMP2-pHluorin and LCa image pairs revealed that, within an observation window of 150 s, discernible LCa puncta transiently existed in close proximity to 38% of fusion sites (149 ± 7 nm, 151 events).

To establish an unbiased correlation between exocytosis and LCa puncta, we aligned and averaged time-lapse image segments of all fusion events and the corresponding LCa signals, using the sharply defined pHluorin peak signals to guide the spatiotemporal alignment. Ensemble averages revealed that exocytosis (n = 467) evoked a focal LCa accumulation that overlapped with the VAMP2-pHluorin peak in space (Figure 1A). The departure time of an LCa punctum from the fusion site (t) was calculated as the interval between the moments that the VAMP2-pHluorin signal reached a peak and the sudden disappearance of the LCa punctum (Figure 1B). We found that the histogram of departure time followed a two-Gaussian distribution, with the centers at 6.9 and 28.9 s (Figure 1C). Thus, direct visualization reveals fast and slow exocytosis-coupled clathrin recruitments.

In addition to the endocytosis of CCPs, some of the LCa puncta disappearance events might have been due to the non-productive disassembly of clathrin clusters (Aguet et al., 2013; Ehrlich et al., 2004; Loerke et al., 2009). To exclude that possibility, we investigated the spatiotemporal correlation of exocytosis with labeled dynamin-1 (Dyn1) (Figure S2A), a mechanochemical enzyme required for the membrane scission (Aguet et al., 2013; Ferguson and De Camilli, 2012). The average Dyn1 signal at fusion sites rose immediately upon fusion (Figure S2B). The subsequent Dyn1 departure displayed fast and slow Gaussian kinetics, with average times of 10.2 and 23.1 s, similar to those of LCa puncta (Figure S2C). These results suggest that the recruitment of LCa to fusion sites and the ensuing fast and slow departures represent coupled CME rather than non-productive events. Collectively, CME is exquisitely orchestrated and spatiotemporally coupled with exocytosis.

By analyzing individual events from time-lapse movies, we identified three elementary types of coupled LCa recruitment. Some LCa puncta resided closely to future fusion sites (~31%, Figure S1A), as if the fusing vesicles directly hit upon pre-existing CCPs, whereas the rest involved LCa puncta either formed de novo at fusion sites (~35%, Figure S1B) or that were rapidly recruited in toto (hopping) from nearby regions to fusion sites (~34%, Figure 1B; Movie S1) after exocytosis. On average, the disappearance of pre-existing LCa puncta from the fusion sites occurred with a mean latency of 13.1 ± 1.6 s (n = 80) after exocytosis and accelerated coupled CME 5- to 7-fold over classical CME (60–100 s in non-excitable cells) (Ehrlich et al., 2004; Loerke et al., 2009; Merrifield et al., 2005). This result agrees with the concept of a readily retrievable pool, in which pre-assembled vesicle membrane proteins wait on the pre-synaptic membrane to be rapidly retrieved after exocytosis (Hua et al., 2011). The coupled endocytosis of CCPs formed de novo at fusion sites was relatively slow (Figure S1B). About 30% of these CCPs did not disappear during the observation window of 150 s, and the other 70% disappeared from the fusion sites at 35.6 ± 3.1 s (n = 61) after exocytosis, which was three times slower than pre-existing LCa puncta ($p < 0.001$). Thus, the exocytosis-coupled de novo CCP formation and ensuing endocytosis operate on a timescale comparable to classical CME (Ehrlich et al., 2004; Loerke et al., 2009; Merrifield et al., 2005).

The discovery of fusion-site-directed, sudden translocation of pre-formed LCa puncta was a surprise, because the CCP might be thought of as an immobile structure where membrane invagination, protein recruitment, and vesicle fission occur at the same location (Ehrlich et al., 2004; Loerke et al., 2009; McMahon and Boucrot, 2011; Merrifield et al., 2005). In search of the possible mechanism, we first quantified the movement of LCa puncta. On average, an LCa punctum traversed 368 ± 32 nm at speeds ranging from 36 nm/s to 1.08 μm/s (n = 74, Figures S1C and S1D), via smooth and sometimes linear trajectories, to reach nascent fusion sites (Figure 1B). Once initiated, this hopping was completed within ~2.2 ± 0.2 s. These characteristics are distinct from the long-range (Keyel et al., 2004), dynactin-dependent fast lateral movement of endosomal clathrin (Zhao et al., 2007). On average, LCa puncta initiated hopping ~15 s after exocytosis, with a broad latency ranging from immediate (2 s, 25th percentile) to delayed (21 s, 75th percentile, Figure S1E), indicating that hopping LCa puncta participate in both the fast and the slow coupled CME. The average departure time was 28.2 ± 2.2 s (exclusive of events outlasting the observation window, Figure 1D), which was ~15 s slower than that of pre-existing CCP-mediated CME but ~7 s faster than that of CCPs formed de novo at fusion sites. Combined, the direct targeting of exocytosis onto sites close to pre-existing CCPs and the lateral hopping of LCa puncta toward fusion sites provide a long-sought local mechanism of rapidly supplying endocytic structures during exocytosis.

Pre-formed CCPs Hop with Cargo Proteins on the Plasma Membrane toward Nascent Fusion Sites for Protein Retrieval

It has been postulated that clathrin can be a component of the fusing granules in retinal bipolar neurons (Pelassa et al., 2014), which may contribute to the hopping LCa puncta and couples CME with exocytosis. We used a fast incidence angle-scanning and azimuthal-averaging TIRF microscope to perform super-resolution reconstruction in the z axis to directly test that possibility (Boulanger et al., 2014; Zong et al., 2014). As shown in Figure 2A, the sudden approaching of a secretory vesicle (labeled with VAMP2-EGFP) along the z axis was not colocalized with any LCa puncta before collapsing into the plasma membrane. After the completion of the exocytosis, a nearby pre-formed LCa punctum, seen only at the plane 0–50 nm beneath the plasma membrane, moved toward the fusion site and docked there. After a delay of ~39 s, the shallow clathrin structure started to invaginate and appeared in the plane that was 100–150 nm beneath the plasma membrane. Finally, it sequentially disappeared from both planes, indicative of internalization of a clathrin-coated vesicle (Figures 2A–2C). This result indicates that hopping LCa puncta represent CCPs associated with the plasma membrane.

Next we explored whether hopping CCPs contain cargo proteins and other membrane components. Synaptotagmin VII (Syt VII) is a vesicular Ca^{2+} sensor mediating glucose-induced insulin secretion (Gustavsson et al., 2008), and it needs to be retrieved from the plasma membrane by CME after vesicle exocytosis (Haucke and De Camilli, 1999). By photo-activating Syt VII-PA-GFP/PA-mCherry under TIRF illumination, we visualized all Syt VII proteins on the plasma membrane as well as a small fraction of vesicular Syt VII close to the plasma membrane; furthermore, by briefly incubating cells with a cell-impermeable dye (30 s), we visualized a fraction of CLIP-Syt VII proteins localized specifically on the plasma membrane. With both protocols, we observed discrete patches of Syt VII left on the cell surface after stimulation (Figure S3A), similar to previous observations in synapses (Hua et al., 2011; Willig et al., 2006). Most Syt VII patches co-localized and laterally moved with LCa puncta on the plasma membrane before ultimately disappearing altogether (Figures 2D, S3B, and S3C; Movie S2). In addition, hopping Syt VII puncta traveled to vesicle fusion sites (Figure 2E) and disappeared there 4.8 or 17.2 s after exocytosis (Figure 2F), qualitatively matching the kinetics of LCa puncta. This demonstrates that clathrin hops to fusion sites along with Syt VII to be internalized together. We also proved that these LCa puncta slid with membrane curvatures. FCHO2 binds and stabilizes shallow curvatures on the surface membrane (Shen et al., 2012). Most LCa puncta co-localized with FCHO2 (71.4% ± 0.9%, seven cells), and many LCa puncta laterally shifted on the plasma membrane with FCHO2 (Figure 2G; Movie S3). The laterally shifted FCHO2 puncta also moved to the fusion sites defined by the transient brightening of the large-dense-core vesicle marker NPY-pHluorin (Figure S4A). Finally, AP2, an adaptor protein critical for the cargo sorting of CCPs, also was found to laterally move on the plasma membrane toward the fusion site after vesicle exocytosis (Figure S4B). Taken together, we conclude that membrane-protein assemblies in toto, i.e., CCPs, hop to the fusion sites to mediate recycling of vesicular proteins.

Cortical Microtubules Provide Tracks for the Hopping of CCPs

The cortical cytoskeleton, which regulates diffusion of membrane receptors on the plasma membrane (Jaqaman et al., 2011), interacts with CCPs (Montagnac et al., 2013). Thus, we

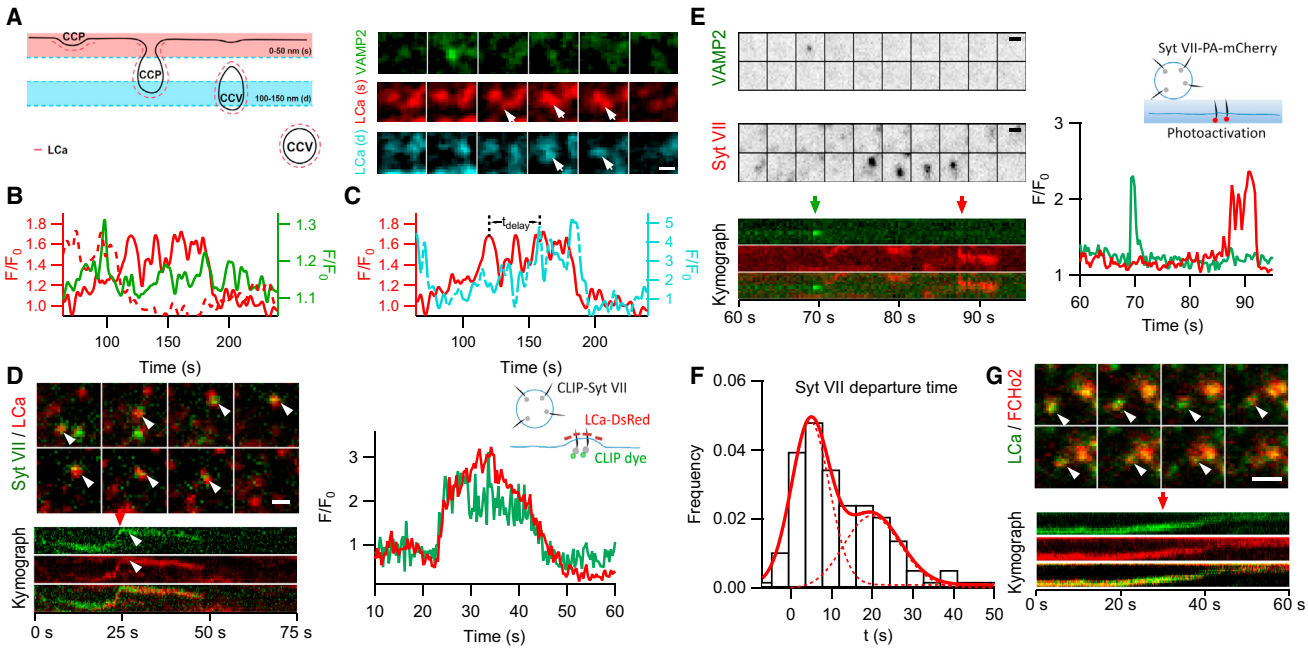

Figure 2. Pre-formed CCPs Hop with Cargo Proteins on the Plasma Membrane toward Nascent Fusion Sites to Be Internalized

(A) A representative example of a vesicle fusion event and correlated hopping LCa puncta event. INS-1 cells were transfected with VAMP2-EGFP and LCa-DsRed, stimulated with 70 mM KCl and 15 mM glucose. (Left) The cartoon shows different clathrin-coated structures visualized by the super-axial resolution incidence angle-scanning and azimuthal-averaging TIRF microscope. (Right) Time-lapse images show the VAMP2-EGFP (green, top) and the LCa signal (red, middle, LCa[s]) at the plane 0–50 nm beneath plasma membrane and the LCa signal at the plane 100–150 nm beneath plasma membrane (blue, bottom, LCa[d]). Montages are shown at 32-s intervals. Arrows indicate the moving CCP.

(B) Time courses of normalized VAMP2-EGFP (green) and LCa (red) signals at the fusion site from the plane 0–50 nm beneath plasma membrane. The dotted line represents the time course of normalized LCa signal at the original site before hopping.

(C) Time courses of normalized LCa signals at the fusion site from the planes 0–50 nm (red) or 100–150 nm (blue dotted) beneath plasma membrane are shown.

(D) A representative example of an LCa/Syt VII co-cluster (arrowheads, top) that migrated on the plasma membrane before disappearing altogether (see also Movie S2). CLIP-Syt VII was labeled with non-permeable CLIP-Surface 488. Montage images are at 19.8, 23.1, 26.4, 33.0, 36.3, 42.9, 46.2, and 49.5 s. Kymographs (bottom) are 3.2 μm high. Red arrow indicates the time point of linear movement; arrowheads indicate sites where intensities are plotted on the right graph. Time courses of normalized Syt VII (green) and LCa (red) signals of the event are shown (right). Inset describes the labeling strategy.

(E) A representative example of a Syt VII cluster that moved to and then disappeared at the fusion site after exocytosis. Time-lapse images of VAMP2-pHluorin (top) and of Syt VII-PA-mCherry signal (middle) at a fusion site are shown at 1.5-s intervals. Kymographs (bottom) are 2.4 μm high. Green arrow, time point of vesicle fusion; red arrow, the starting time point of Syt VII movement. Time courses of normalized fluorescence signals are shown (right). Inset describes the labeling strategy.

(F) Histogram of Syt VII cluster departure times (t) at fusion sites is shown (n = 144).

(G) A representative example of a hopping CCP (LCa-EGFP, arrowheads) that co-localized with an FCHO2-mCherry punctum, migrated on the plasma membrane before disappearing altogether (see also Movie S3). Montage images (top) are at 3-s intervals. Kymographs (bottom) are 1.7 μm high. Red arrow marks the initiation of LCa/FCHO2 movement. Scale bars. 500 nm (A) and 1 μm (D, E, and G). See also Figure S3 for the co-localization and co-movement of plasma membrane-associated Syt VII with CCPs and Figure S4 for the hopping of other adaptor proteins of CCP toward nascent fusion sites labeled by different markers.

hypothesized that the cytoskeletal network immediately beneath the plasma membrane might provide tracks for the CCP hopping. By labeling microtubules with EGFP-Tubulin, we observed that a CCP moved along a cortical microtubule filament and stalled at the intersection of two filaments; as this microtubule re-oriented, the CCP went along with the sliding filament (Figure 3A; Movie S4). To quantitatively correlate CCP motions with cytoskeleton network, we tracked trajectories of all CCPs and identified ~10% linearly moving CCPs, using methods proposed previously (Jaqaman et al., 2008, 2011; Figures 3B [inset] and 3C). These linear CCP movements were preferentially overlapped with cortical microtubules more than with actin filaments (labeled with Lifeact-EGFP, Figure 3B). Consistently, the proportion of CCPs that exhibited linear motion was reduced by disruption of the microtubular network with nocodazole, but not by depolymerization of filamentous actin with either cytochalasin D (CytoD) or latrunculin A (Figures 3C and S5A). This is different from the actin-dependent lateral movement of clathrin structures reported previously (Gaidarov et al., 1999). We propose that CCP hopping is a subset of linear CCP movements, since nocodazole treatment reduced both the overall CCP recruitment and the hopping of CCPs to fusion sites, whereas CytoD treatment reduced neither (Figures 3D and 3E). In addition, inhibition of kinesin 5, dynactin, or myosin 5 all failed to reduce the linearly motile population of CCPs (Figure 3C). Given the relatively slow speed of CCP hopping (Figure S1D), these results suggest that linear CCP motion is unlikely to be regulated by classical motor proteins, but may result from an association of CCPs with dynamic cortical microtubules (Montagnac et al., 2013).

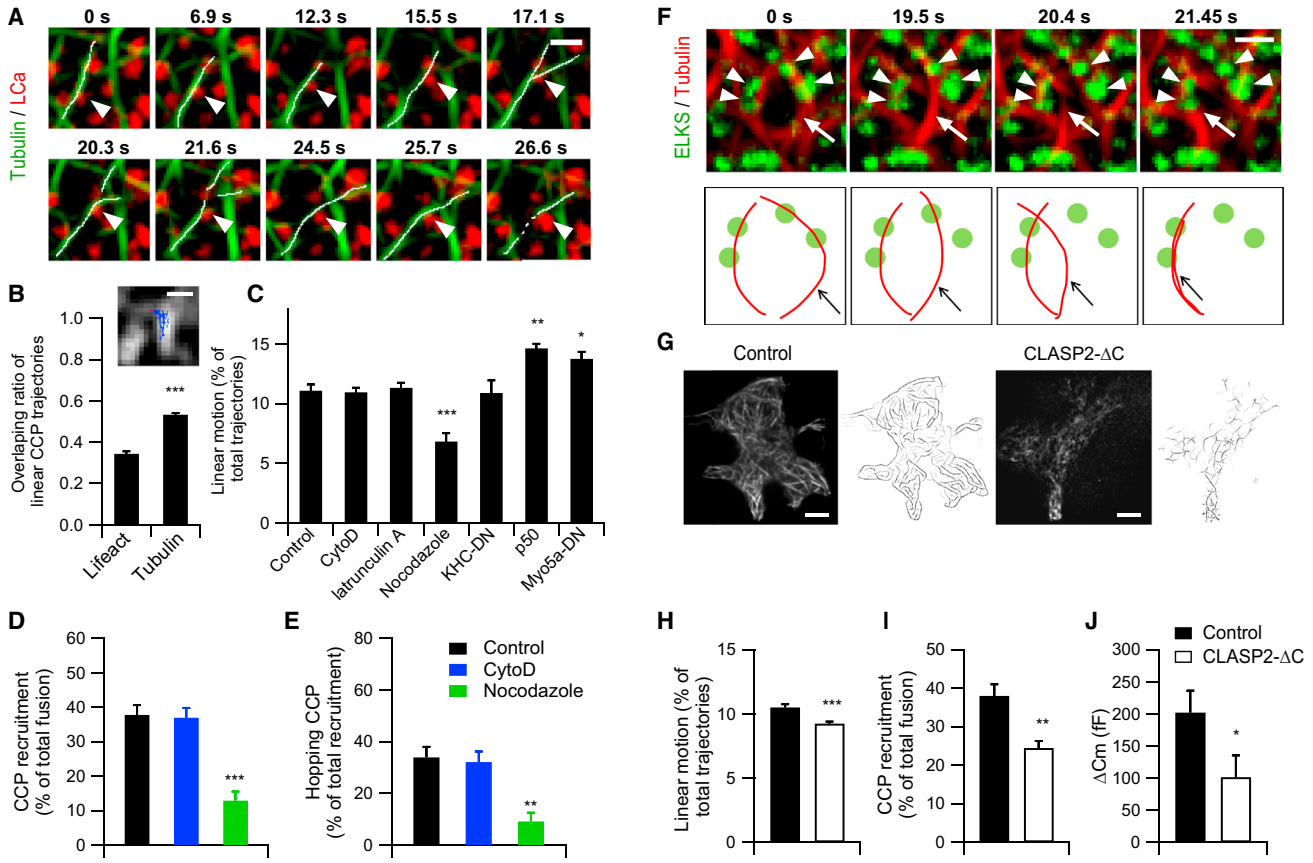

Figure 3. CLASP Mediates the Anchoring of Cortical Microtubules on the Surface Membrane, which Regulates Both Lateral Movement of CCPs and Regulated Exocytosis

(A) Time-lapse images show a mobile CCP (LCa-DsRed, arrowheads) moving along a dynamic microtubule filament (EGFP-Tubulin, white line) and then being redirected by the sliding microtubule. See also Movie S4.

(B) The ratios of linear CCP trajectories overlapped with actin filaments (Lifeact-EGFP, 3,817 trajectories from six cells) or microtubules (EGFP-Tubulin, 8,262 trajectories from nine cells, $p < 0.001$). Inset shows representative linear CCP trajectory (blue) overlaid on EGFP-Tubulin (white).

(C) Percentages of linearly moving CCPs in LCa-DsRed-expressing control cells (n = 14); in LCa-DsRed-expressing cells incubated with CytoD (20 μM, 20 min, n = 16), latrunculin A (10 μM, 30 min, n = 27), or nocodazole (10 μM, 2 hr, n = 7, $p < 0.001$); or in LCa-DsRed-expressing cells co-transfected with KHC-DN (n = 4), p50 (n = 7, $p < 0.01$), or myo5a-DN (n = 9, $p < 0.05$), which inhibit kinesin, dynein, or myosin5, respectively. Unless specified otherwise, all statistical differences are between the control cells and the designated treated cells.

(D) The percentage of exocytosis associated with CCP recruitment in control cells (n = 6) and cells pre-treated with CytoD (n = 5) or nocodazole (n = 5, $p < 0.001$) is shown.

(E) The percentage of hopping CCP among the total CCP recruitment at fusion sites in control cells (n = 6) and cells pre-treated with CytoD (n = 5) or nocodazole (n = 5, $p < 0.01$) is shown.

(F) An example of a microtubule filament (TagRFP-T-Tubulin, arrows) sliding back and forth between two pairs of ELKS puncta (GFP-ELKS, arrowheads) upon stimulation is shown. See also Movie S5. Simplified cartoons are shown (bottom).

(G) Microtubule network and their skeletal extraction pictures of microtubule filaments under TIRF illumination in control cells (INS-1 cells transfected with EGFP-Tubulin, left) and cells co-transfected with EGFP-Tubulin and mTagBFP2-CLASP2-ΔC (right) are shown.

(H) The percentage of linearly moving CCPs in control cells (n = 8) and cells overexpressing CLASP2-ΔC (n = 9, $p < 0.001$) is shown.

(I) The percentage of exocytosis associated with CCP recruitment in control cells (n = 19) and cells overexpressing CLASP2-ΔC (n = 8, $p < 0.01$) is shown.

(J) The membrane capacitance increment evoked by trains of depolarization in control cells (n = 10) and cells overexpressing CLASP2-ΔC (n = 7, $p < 0.05$) is shown. Scale bars, 1 μm (A), 500 nm (B), 2 μm (F), and 5 μm (G). See also Figure S5A for the disruption of actin filament by CytoD or latrunculin A treatment, Figures S5B–S5D for the stimulation-evoked accumulation of LL5β/ELKS clusters on the plasma membrane, and Figure S5E for the capacitance traces in control cells and in cells transfected with CLASP2-ΔC mutant.

Next we tried to search for proteins anchoring cortical microtubules to the plasma membrane. Microtubule filaments are found in close proximity to the active zone in synapses (Westrum and Gray, 1986), and they are attached to the cell cortex via the interaction of cytoplasmic linker-associated protein (CLASP) on the microtubules with LL5β/ELKS on the plasma membrane in HeLa cells (Lansbergen et al., 2006). In INS-1 cells co-transfected with TagRFP-T-Tubulin and EGFP-ELKS, we found that most cortical microtubules traversed ELKS puncta; after stimulation, more LL5β/ELKS puncta appeared on the plasma membrane (Figures S5B–S5D). Correspondingly, segmented filaments frequently slid between different pairs of ELKS puncta

(Figure 3F; Movie S5). In cells transfected with a CLASP2 truncation mutant (CLASP2-ΔC) that is unable to interact with the LL5β/ELKS complex (Lansbergen et al., 2006), cortical microtubules were reduced (Figure 3G), and both the linear CCP movement and the exocytosis-coupled CCP recruitment at fusion sites were inhibited (Figures 3H and 3I). Depolarization-evoked exocytosis also was inhibited in these cells (Figures 3J and S5E), supporting a role of CLASP and ELKS in regulated exocytosis as shown previously in synapses and endocrine cells (Beffert et al., 2012; Haucke et al., 2011; Ohara-Imaizumi et al., 2005). Taken together, the dynamic, CLASP-dependent anchoring of cortical microtubules to the plasma membrane constitutes an exo-endocytosis coupling factor.

Local, Transient DAG Gradients Convey the Spatial Orientation for the Hopping of CCPs

To initiate and direct CCP hopping along the microtubular track, the triggering signal must be exocytosis specific, local, and transient. In this regard, depolarization-triggered Ca^{2+} influx that is required for exocytosis may activate phospholipase C, which hydrolyzes phosphatidylinositol 4,5-bisphosphate to generate DAG (Kadamur and Ross, 2013). DAG is a non-bilayer lipid with a negative curvature (Carrasco and Mérida, 2007), and its accumulation may reduce the elastic energy of membrane deformation and facilitate lateral CCP movement. Therefore, we used the EGFP-tagged tandem C1 domains of protein kinase D (PKD) as a DAG indicator (PKD-C1ab-EGFP) (Kim et al., 2011), and we tested whether the local DAG gradient could be a triggering signal. Global increases in DAG concentration were detected in cells stimulated with carbachol (Figure S6). More importantly, by spatiotemporal averaging, we found that the local DAG concentration began to increase at the fusion sites prior to exocytosis, reached a plateau when the fusion pores fully opened, and stayed elevated for some time after exocytosis (Figures 4A and 4B). Incubating cells with a DAG analog, 1-oleoyl-2-acetyl-sn-glycerol (OAG), reduced the surface membrane tension as measured by optical tweezers (Figures 4C–4E) and increased the speed of linear CCP movement (Figure 4F). In contrast, inhibition of phospholipase C with U73122, which blocked DAG generation, reduced the speed of linear CCP movement (Figure 4G). The speed of linearly moving CCPs was consistently faster close to the fusion sites than elsewhere (Figure 4H). Hence, our data suggest that the exocytosis-associated local DAG gradient initiates and directs the hopping of CCPs toward nascent fusion sites by reducing the energy barrier against intra-membrane movement of CCPs. This also highlights a general, unappreciated role of membrane microdomains with transient curvatures: they may attract curved sub-cellular structures in addition to the recruitment of cytosolic proteins with curvatures as proposed recently (Galic et al., 2012).

Exocytosis-Coupled CME Contributes to the Fast Recycling of Both Plasma Membrane and Vesicular Proteins

In pancreatic β cells, membrane depolarization triggers CME and clathrin-independent endocytosis; both processes are dynamin dependent (He et al., 2008). Thus, we used pitstop (von Kleist et al., 2011) to block CME and dynasore (Macia et al., 2006) to block CME plus clathrin-independent endocytosis. Using repetitive trains of depolarization in control cells and in cells pretreated with either pitstop or dynasore, we examined evoked exocytosis and endocytosis. Inhibition of cellular dynamin function with dynasore eliminated most of the exocytosis-coupled endocytosis (Figures 5A, 5B, and 5D). Pitstop pretreatment increased the time constant of the fast capacitance decay (control: 0.35 ± 0.04 s, n = 8; pitstop treated: 0.66 ± 0.08 s, n = 8, $p < 0.01$) (Figure 5A), and it reduced the membrane retrieval within 4 s after a train of depolarization by half (Figure 5D). Combined, CME contributes to ~50% of the fast membrane retrieval after exocytosis. On the other hand, inhibition of CME failed to affect exocytosis evoked by the first train of depolarization, but significantly inhibited subsequent exocytosis evoked by the fourth and fifth trains of depolarization (Figures 5A–5C). Inhibition of coupled endocytosis also reduces the fast release of synaptic vesicles evoked by repetitive stimulations delivered at intervals less than ~10 s in Calyx synapses (Hosoi et al., 2009). Therefore, fast coupled CME plays an important role in sustaining multiple rounds of exocytosis during prolonged stimulations in neurons and endocrine cells, as proposed previously (Neher, 2010).

Next we explored how CME contributed to the vesicular protein recycling process by studying endocytosis of surface VAMP2 protein tagged with fluorogen-activating protein (FAP) (Szent-Gyorgyi et al., 2008). Because the fluorogen dye alone remains dark until binding to the FAP, its fluorescence intensity is directly correlated with the amount of VAMP2-FAP protein labeled. Using a cell non-permeable αRED fluorogen, we found that surface VAMP2-FAP was internalized and transported to puncta and Golgi-like structures in the cytosol during 10 min of stimulation. In contrast, most recycling of VAMP2 protein after stimulation was blocked in cells pretreated with pitstop, while dynasore pretreatment only slightly enhanced the accumulation of VAMP2-FAP on the plasma membrane than pitstop pretreatment (Figures 5E and 5F). Therefore, although CME only acts as a complementary route of plasma membrane retrieval, it plays a dominant role in the recycling of VAMP2 protein on the plasma membrane.

DISCUSSION

Overall, we have unraveled an exquisite, DAG-guided and microtubule-assisted mechanism for the spatiotemporal regulation of exo-endocytosis coupling in excitable cells. We envision that pre-formed CCPs are motile structures on the plasma membrane. Excitable cells make use of these pre-formed CCPs to accelerate exocytosis-coupled CME, both by directly targeting them close to fusion sites and by moving them from nearby regions. Upon stimulation, pre-formed CCPs laterally hop along dynamic cortical microtubules mediated by CLASP on the microtubules and LL5β/ELKS on the surface membrane, and they are driven by a transient, local DAG gradient toward nascent fusion sites (Figure 6). This enables CCPs that initially assembled at spatially randomized sites to retrieve vesicle membrane proteins at preferred nascent fusion sites in a timely fashion.

Now we have shown that exocytosis-coupled CME and clathrin-independent endocytosis each contributed to ~50% of the fast membrane retrieval after depolarization (Figure 5D). In contrast, almost all of the VAMP2 internalization after stimulation was mediated by coupled CME (Figures 5E and 5F). These data

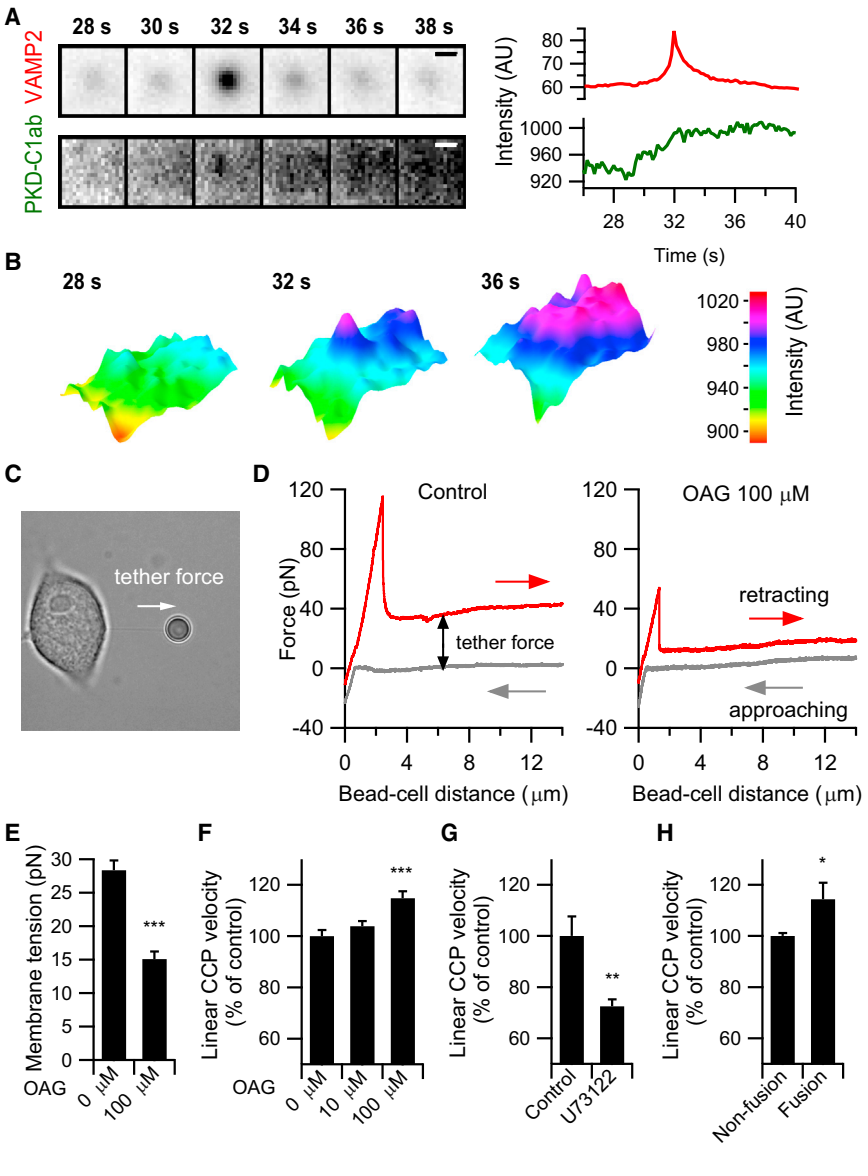

Figure 4. Local DAG Gradient Generated upon Exocytosis Directs the Hopping of CCPs toward Nascent Fusion Sites

(A) Local DAG indicated by PKD-C1ab-GFP transiently accumulated at vesicle fusion sites indicated by VAMP2-mOrange2. Time-lapse images show the average VAMP2-mOrange2 signal (of 193 fusion events, top) and the corresponding average DAG signal (bottom) at fusion sites. Scale bars, 500 nm. Time courses of average fluorescence signals are shown (right).

(B) Surface plots of the mean DAG gradient (colormap coded) around fusion sites at times before (28 s), during (32 s), and after exocytosis (36 s) are shown.

(C) A representative example of a membrane tether formed as the bead was retracted away from the cell is shown.

(D) Examples show tether force versus distance from a control INS-1 cell (left) and an OAG-treated cell (100 μM, right). Red, the force required for retracting the bead away from the cell at a speed of 1 μm/s; gray, the baseline force required for moving the bead toward the cell at 1 μm/s. The difference between these two forces is the calibrated tether force.

(E) Surface membrane tension measured by optical tweezers in control (n = 32) and OAG-treated (100 μM, 15–20 min, n = 32, $p < 0.001$) cells is shown.

(F) The velocity of linear CCP movement in OAG-treated cells as compared to the control. INS-1 cells were stimulated with high KCl and high glucose in absence or presence of OAG (0 μM as control, mean velocity of linear CCP movement, 598 ± 14 nm/s, 2,704 trajectories from nine cells; 10 μM, 2,724 trajectories from nine cells; 100 μM, 4,451 trajectories from twelve cells, $p < 0.001$).

(G) The velocity of linear CCP movement in cells pre-incubated with the phospholipase C inhibitor U73122 (10 μM) for 15 min (3,447 trajectories from eight cells) as compared to control cells (mean velocity of linear CCP movement, 532 ± 40 nm/s, 1,142 trajectories from four cells, $p < 0.01$) is shown.

(H) Linear movement of CCPs at fusion sites (27 trajectories) compared to that at random, non-fusion sites (control, mean velocity of linear CCP movement, 543 ± 6 nm/s, 1,256 trajectories, $p < 0.05$). See also Figure S6 for the global increase in cellular DAG concentration detected by PKD-C1ab-GFP upon carbachol stimulation.

highlight a selective recycling of vesicular proteins via fast exocytosis-coupled CME. Conceptually, lateral hopping of CCPs represents an active paradigm in retrieving vesicular proteins on the plasma membrane, in contrast to the conventional view of CCPs as spatially stationary pits that passively collect cargos passing by. By moving toward nascent vesicle fusion sites enriched with cargo proteins, shallow CCPs may act as an active sorting machinery to recruit vesicular proteins, especially for those non-diffusing ones such as phogrin (Tsuboi et al., 2004). The merge of shallow CCPs with cargos reduces abortive CCP events and facilitates CCP maturation and effective endocytosis, as others have suggested (Swan, 2013). Although pre-existing CCPs and de novo formation of CCPs at fusion sites share some of these advantages, only hopping CCPs can rapidly and continuously supply partially assembled endocytic machinery to the vesicle release sites. As compared to the control, exocytosis evoked by repetitive stimulations was gradually reduced in cells with compromised CME, and the reduction started to reach statistical significance at the fourth train of depolarization (Figures 5A–5C). Given that the reduced exocytosis is mostly likely to be due to the disruption of fusion sites by prior exocytosis, our data further support that hopping CCPs may be important for the local, fast, and efficient clearance of vesicular components left at the fusion sites during repetitive stimulations.

The microtubule-dependent linear movement of CCP is intriguing. It may be a passive process through which the sliding microtubules push CCPs attached to them toward fusion sites. The α-tubulin acetyltransferase (αTAT1) in the CCPs, which acetylates and stabilizes the microtubules (Montagnac et al., 2013), could be the physical linker between microtubules and CCPs.

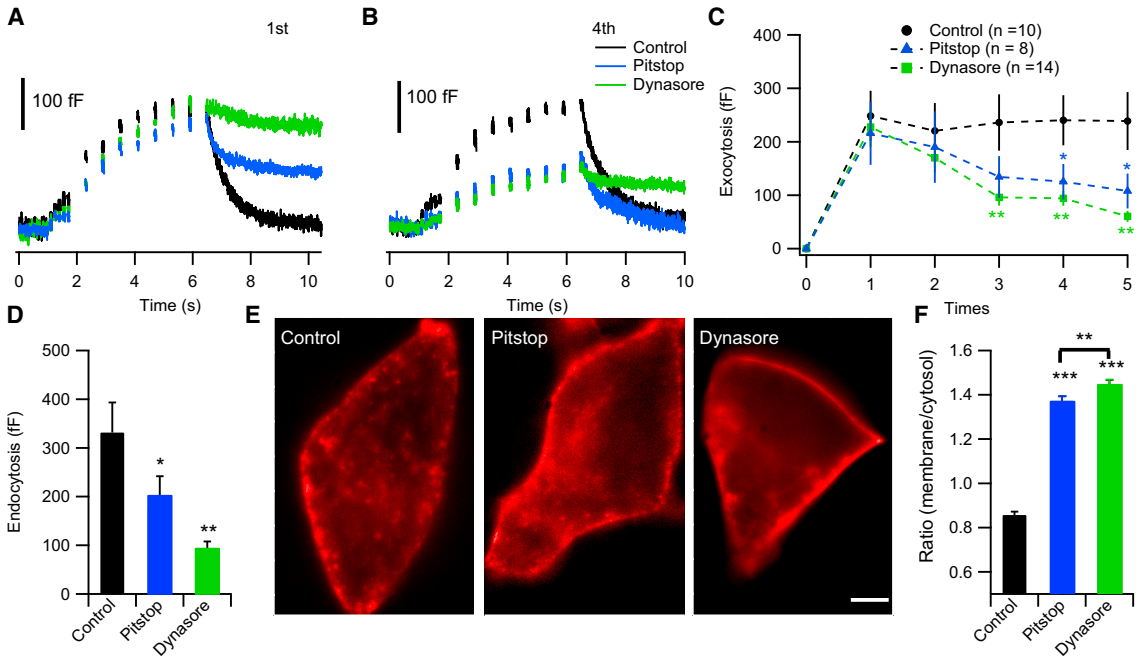

Figure 5. Inhibition of CME Significantly Reduced Recycling of Plasma Membrane, Vesicular Proteins, and Local Clearance of Fusion Sites upon Repetitive Stimulations

Five consecutive rounds of depolarization stimulations were delivered to control INS-1 cells (n = 10, black) and INS-1 cells pretreated with either pitstop (24 μM, 10 min, n = 8, blue) or dynasore (80 μM, 10 min, n = 14, green). The time interval between different rounds of depolarization was 5 s.

(A and B) The average increases and decreases in membrane capacitance evoked by the first depolarization stimulation (A) and by the fourth depolarization stimulation (B) are shown.

(C) Evoked exocytosis from control INS-1 cells and INS-1 cells pretreated with either pitstop or dynasore during five consecutive rounds of depolarization stimulations are shown (statistical significances as indicated on the graph).

(D) Within 4 s after the very first depolarization, evoked endocytosis in control INS-1 cells and INS-1 cells pretreated with either pitstop or dynasore were calculated as decreases in membrane capacitance from 6.2 to 10.2 s in (A).

(E) Representative images show INS-1 cells transfected with VAMP2-FAP (red) treated with 70 mM KCl, 15 mM glucose solution containing DMSO vehicle (0.8%), pitstop (25 μM), or dynasore (80 μM) for 10 min. Scale bar, 5 μm.

(F) The recycling efficiency of VAMP2, quantified as a ratio of average fluorescence intensities of the whole cell boundary to that of the cell cytosol, in a cell treated with 0.8% DMSO (n = 120), pitstop (n = 144, $p < 0.001$), or dynasore (n = 132, $p < 0.001$). The difference in the VAMP2 recycling is also significant between pitstop-treated cells and dynasore-treated cells ($p < 0.01$).

Alternatively, cortical microtubule filaments could serve as cages that convert random CCP mobility into linear motion, similar to the linear diffusion of CD36 receptors on the plasma membrane due to the cytoskeletal confinement (Jaqaman et al., 2011). Further work is needed to delineate these possibilities. Nevertheless, we did observe an increase in the number of ELKS clusters on the plasma membrane upon stimulation (Figures S5B–S5D), which was accomplished with dynamic reorganization of cortical microtubule networks (Figure 3F). Moreover, CLASP-dependent anchoring of cortical microtubules to the plasma membrane were required for vesicle fusions, linear CCP motion, and CCP recruitment at fusion sites (Figures 3H–3J). Thus, the three-dimensional cortical microtubules anchored around ELKS-defined fusion sites may represent a spatiotemporal coupling framework, which increases the probability of cargo proteins merging with mobile CCPs and enables efficient clearance of plasma membrane at fusion sites.

Although this study was conducted in an endocrine cell, functions of the proteins involved (such as ELKS and CLASP) are conserved in synapses, suggesting that a conserved mechanism also may account for the fast CME critical for the sustained neurotransmission in synapses (Kawasaki et al., 2011). Moreover, the transient increase in DAG on the plasma membrane close to exocytic sites observed here also may facilitate generation of clathrin-independent invaginations observed shortly after depolarization in synapses (Kononenko et al., 2014; Watanabe et al., 2013). The microtubule-dependent movement of CCPs facilitates active sorting of vesicle membrane proteins on the plasma membrane toward designated sites to be internalized, which also may participate in other extracellular signal-regulated fine-tuning of cell membrane components in other eukaryotic cells.

EXPERIMENTAL PROCEDURES

Live-Cell Imaging and Fluorescence Microscopy

All experiments were performed at 37°C. INS-1 cells were planted on glass coverslips and incubated with bath solution containing the following (in mM): 136 NaCl, 4.2 KCl, 2.4 $CaCl_2$, 1.2 KH_2PO_4, 1.2 $MgSO_4$, 4 glucose, 10 HEPES, and 1 L-glutamine (pH 7.4). Individual coverslips were then placed in a metal chamber mounted on a heated stage. Unless specified otherwise, INS-1 cells were stimulated with a solution containing the following (in mM): 70 NaCl, 70 KCl, 2.4 $CaCl_2$, 1.2 KH_2PO_4, 1.2 $MgSO_4$, 15 glucose, 10 HEPES, and 1 L-glutamine (pH 7.4) to trigger exocytosis and endocytosis.

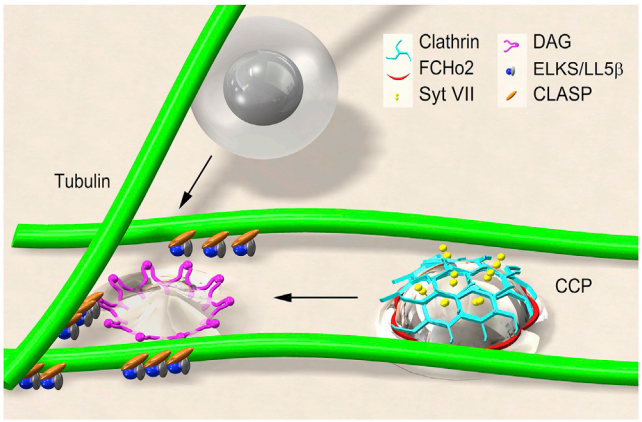

Figure 6. Model of How Fast CME Is Coupled with Regulated Exocytosis

The local DAG gradient steers the hopping of a mobile CCP toward the fusion site along tracks provided by cortical microtubule filaments, which also help the delivery of secretory vesicles to fuse with the plasma membrane.

For Figures 1, 2D–2F, and S1–S3, a TIRF microscope was equipped with a Sensicam EM682KX camera (PCO AG) and a 100× 1.49 numerical aperture (NA) oil-immersion TIRF objective (Olympus). Most images were acquired at 2 Hz, except for Figures 2D, 2E, and S3 (3.3 Hz). Each pixel from the camera was 67 × 67 nm.

A different TIRF setup was used for Figures 2G, 3, 4, 5, and S4–S6. We used an Olympus IX81 inverted microscope equipped with a 150× 1.45 NA oil-immersion TIRF objective (Olympus). Fluorescence signals were acquired using an electron-multiplying charge-coupled device (EMCCD, Andor iXon3 888) at a sampling rate of 6.7 Hz controlled by MetaMorph (Molecular Devices). Each pixel from the Andor camera was 87 × 87 nm. A 473-nm laser was used to excite GFP/pHluorin, a 561-nm laser to excite mCherry/RFP/DsRed/TagRFP-T, and a 405-nm laser to excite mTagBFP2. For two-color imaging, 100-nm fluorescent beads (TetraSpecK Microspheres, Life Technologies) were deposited onto a coverslip and imaged as markers for later alignment. To visualize surface VAMP2-FAP internalization (Figure 5E), the TIRF illumination was adjusted to wide field.

The fast incidence angle-scanning and azimuthal-averaging TIRF microscope was built on a commercial microscopy (IX81, Olympus) equipped with an apochromatic objective lens (APO 100×/1.65 NA, Olympus) (Figures 2A–2C). Two excitation lasers (Sapphire 488LP and Sapphire 561LP, Coherent) were collimated and combined by an AOTF and projected onto a two-axis MEMS (A1B2.2, Mirrorcle Tech), which enabled fast incidence angle scanning or the scanning of a circle at the back focal plane of the objective for azimuthal averaging at 1 kHz. The emitted fluorescence was captured by an EMCCD camera (iXon 897U, Andor). The whole system was controlled by Labview (Zong et al., 2014). Cells were cultured on customized N-LAF21 coverslip with an index of refraction of 1.78. To achieve 50-nm axial resolution, sequential dual-color TIRF imaging at ten different incidence angles (51.34, 51.45, 51.59, 51.795, 52.085, 52.54, 53.29, 54.67, 57.72, and 67.38) were recorded at a frequency of 0.8 s/vol. Image reconstruction was conducted as reported previously (Boulanger et al., 2014).

Visualization of Surface VAMP2-FAP Internalization

In experiments aimed to visualize VAMP2-FAP internalization, INS-1 cells were transfected with VAMP2-FAP vector and labeled with a bath solution containing 70 mM KCl, 15 mM glucose, and non-permeable αRED fluorogen (100 nM, SpectraGenetics) for 10 min at 37°C. These cells were transferred to an imaging chamber without washing and imaged under wide-field illumination.

Selectively Highlighting or Labeling Surface Syt VII

Two methods were used to label the surface pool of Syt VII. In experiments using Syt VII-PA-GFP/PA-mCherry (Figures 2E, 2F, and S3C), cells were first illuminated with a 405-nm laser for 15 s to photo-activate the Syt VII population close to the cell surface and then imaged during stimulation. In experiments using CLIP-Syt VII, cells were first incubated in a stimulation solution containing KCl, glucose, and non-permeable CLIP-Surface 488 (New England Biolabs) (Figures 2D, S3A, and 3B; 20 mM) for 30 s, which was used to label the surface pool of Syt VII that was transiently inserted into the plasma membrane due to vesicle exocytosis. Cells were then washed three times in normal bath solution for 2 min before imaging under stimulation with a solution containing KCl and glucose.

Electrophysiology

Electrophysiological experiments were conducted by standard whole-cell recording using an EPC-10 patch-clamp amplifier (HEKA) as previously described (Liang et al., 2011). The capacitance was measured using the sine + DC mode of the lock-in extension in the Pulse software, with an 800-Hz, 20-mV peak-to-peak sinusoid voltage applied onto a DC holding potential of −70 mV. In Figure 5, the intracellular pipette solution contained the following (in mM): 125 Cs-glutamate, 10 NaCl, 0.05 EGTA, 1 $MgCl_2$, and 5 HEPES, with pH adjusted to 7.35 using CsOH. Five trains of stimulation were sequentially delivered to the control cells or cells pretreated with inhibitors. Each train of stimulation (Cm5+8) consisted of five 50-ms and eight 500-ms depolarizations (from −70 to 0 mV) to evoke release from the immediately releasable pool (IRP) and the readily releasable pool (RRP) of vesicles, respectively. The inter-pulse interval was 100 ms (Merrins and Stuenkel, 2008) and the time interval between each train of stimulation was 5 s. The exocytosis was calculated as the increase in membrane capacitance at the end of eight 500-ms depolarization, and the endocytosis was calculated as the decrease in membrane capacitance at 4 s after depolarization as compared to that at the end of depolarization. The decays in membrane capacitance were fitted with either single or double exponential functions to extract time constants of the fast and the slow endocytosis, as shown previously (He et al., 2008). In Figure S5E, the pipette solution contained the following (in mM): 125 Cs-glutamate, 2 Mg-ATP, 0.3 Na_2-GTP, 1 $MgCl_2$, and 0.1 EGTA (pH 7.2 adjusted with CsOH). Capacitance increases were evoked by eight trains of depolarization (from −70 to 0 mV for 500 ms).

Optical Tweezer Experiments

The JPK NanoTracker optical tweezers system was used to measure the membrane tether force, which indicates the cell membrane tension. Data were collected and calibrated using the PFM Software Release 2.2 equipped with the JPK system. To form a tether, a 4-μm polystyrene bead approached the cell at 1 μm/s, arrived at the cell surface, stopped for 10 s for attachment, and then was retracted at 1 μm/s.

Imaging Data Analysis

Alignment of two-color images, semi-automated vesicle-fusion detection, and spatiotemporal averaging of local fluorescence signals from multiple events were done using a self-written program in MATLAB (MathWorks) (Yuan et al., 2015). A 5-pixel (335-nm) diameter circle that encloses the center of a fusion spot was selected to calculate the average fluorescence signal of VAMP2-pHluorin. LCa-DsRed or Dyn1-mKO signals were calculated from the same spot, accordingly, and fluorescence intensity changes above 10% of the original base value were considered positive for recruitment of the marker. The distance between a local maximum VAMP2-pHluorin signal and the neighboring LCa punctum was calculated for each fusion event that recruited endocytic markers. The departure time (t) was defined as the time difference between the opening of the fusion pore (as indicated by an increase in the fluorescence intensity of pHluorin) and the decrease of the LCa/Dyn1/Syt VII puncta signal (Figure 1B). The histograms of t were fitted with a Gaussian function (fast population) plus one or two Rayleigh functions (slow populations) (Loerke et al., 2009).

To obtain spatiotemporal averages, all exocytic events were aligned temporally according to the frame that exhibited maximum pHluorin fluorescence intensity and spatially according to the weighted centroid of the punctum. Correspondingly, local endocytic signals (LCa/Dyn1) and the DAG signal (PKD-C1ab-GFP) from the other channel were spatiotemporally aligned according to the same time and position. For comparison, the same number of signals from the other channel at random frames and sites that was not co-localized with exocytosis also were aligned and averaged.

To detect CCPs, we first de-noised images with a wavelet transform function (Olivo-Marin, 2002), determined positions of puncta by finding local maxima with a mask of 5 × 5 pixels, and then calculated weighted centroids of these puncta to yield sub-pixel accuracy. Single-particle tracking was accomplished using spatially and temporally global particle assignment, as described previously (Jaqaman et al., 2008). Tracks with lengths above ten frames were kept and classified as either linear or confined CCP diffusion based on a statistical testing algorithm, as previously described (Jaqaman et al., 2011). Once the trajectory of a CCP intersected within 5 pixels from any fusion site, it was considered as possibly related to exocytosis, while others were regarded as unrelated to exocytosis. Based on these criteria, we compared average velocities of CCPs that were related and unrelated to exocytosis (Figure 4H).

Analysis of microtubule images was performed with Fiji (ImageJ). They were first de-convolved using the Richardson-Lucy algorithm (Vonesch and Unser, 2008), background subtracted (rolling ball radius = 20), and then filtered using the steerable plugin (Aguet et al., 2005).

Statistical Analysis

All data were analyzed and final images were prepared using Igor Pro software (Wavemetrics). Average results are presented as the mean value ± SEM from the number of experiments indicated. Statistical significance was evaluated using either Student's t test for single Gaussian-distributed datasets or the Mann-Whitney rank-sum test for non-single Gaussian-distributed datasets (*, **, and *** denote p values < 0.05, 0.01, and 0.001, respectively).

SUPPLEMENTAL INFORMATION

Supplemental Information includes Supplemental Experimental Procedures, six figures, and five movies and can be found with this article online at http://dx.doi.org/10.1016/j.devcel.2015.09.004.

AUTHOR CONTRIBUTIONS

Conceptualization, L.C.; Methodology, T.Y., L.L., L.W., and X.H.; Software, Y.Z., J.B., C.G., and J.S; Validation, L.X., J.L., W.D., and L.Y.; Investigation, T.Y., L.C., L.L., L.W., X.Z., and S.Z.; Resources, J.L.; Visualization, W.Z. and T.Y.; Data Curation: T.Y. and Y.Z.; Writing – Original Draft, L.C.; Writing – Review & Editing, L.C. and Y.L.; Supervision, L.C. and Y.L.; Funding Acquisition, L.C., Y.L., and J.S.

ACKNOWLEDGMENTS

We thank Professors M. McNiven, J. Lippincott-Schwartz, V. Verkhusha, D. Arnold, H. Gerdes, R. Vallee, F. Meunier, T. Balla, R. Tsien, A. Akhmanova, M. Davidson, T. Kirchhausen, and C. Merrifield for plasmids. We thank Professor H. Cheng for his discussions during the preparation of this paper, and Professors B. Hille, D. Koh, I. Bruce, and Z. Wu and Dr. S. Jung for their critical comments on the manuscript. This work was supported by grants from the National Science Foundation of China (81222020, 31221002, 31327901, 31570839, and 31301186), the Beijing Municipal Science & Technology Commission (7121008), the Major State Basic Research Program of P.R. China (2013CB531200), and the National Key Technology R&D Program (SQ2011SF11B01041). The PICT Cell and Tissue Imaging Core Facility of the Institut Curie is part of the France-BioImaging national infrastructure supported by the French National Research Agency (ANR-10-INBS-04, PIA).

Received: March 9, 2015
Revised: August 5, 2015
Accepted: September 10, 2015
Published: October 1, 2015

REFERENCES

Aguet, F., Jacob, M., and Unser, M. (2005). Three-dimensional feature detection using optimal steerable filters. 2005 International Conference on Image Processing (ICIP), Vols 1–5, 2109–2112.

Aguet, F., Antonescu, C.N., Mettlen, M., Schmid, S.L., and Danuser, G. (2013). Advances in analysis of low signal-to-noise images link dynamin and AP2 to the functions of an endocytic checkpoint. Dev. Cell *26*, 279–291.

Allersma, M.W., Wang, L., Axelrod, D., and Holz, R.W. (2004). Visualization of regulated exocytosis with a granule-membrane probe using total internal reflection microscopy. Mol. Biol. Cell *15*, 4658–4668.

Artalejo, C.R., Elhamdani, A., and Palfrey, H.C. (2002). Sustained stimulation shifts the mechanism of endocytosis from dynamin-1-dependent rapid endocytosis to clathrin- and dynamin-2-mediated slow endocytosis in chromaffin cells. Proc. Natl. Acad. Sci. USA *99*, 6358–6363.

Beffert, U., Dillon, G.M., Sullivan, J.M., Stuart, C.E., Gilbert, J.P., Kambouris, J.A., and Ho, A. (2012). Microtubule plus-end tracking protein CLASP2 regulates neuronal polarity and synaptic function. J. Neurosci. *32*, 13906–13916.

Boulanger, J., Gueudry, C., Münch, D., Cinquin, B., Paul-Gilloteaux, P., Bardin, S., Guérin, C., Senger, F., Blanchoin, L., and Salamero, J. (2014). Fast high-resolution 3D total internal reflection fluorescence microscopy by incidence angle scanning and azimuthal averaging. Proc. Natl. Acad. Sci. USA *111*, 17164–17169.

Carrasco, S., and Mérida, I. (2007). Diacylglycerol, when simplicity becomes complex. Trends Biochem. Sci. *32*, 27–36.

Ehrlich, M., Boll, W., Van Oijen, A., Hariharan, R., Chandran, K., Nibert, M.L., and Kirchhausen, T. (2004). Endocytosis by random initiation and stabilization of clathrin-coated pits. Cell *118*, 591–605.

Ferguson, S.M., and De Camilli, P. (2012). Dynamin, a membrane-remodelling GTPase. Nat. Rev. Mol. Cell Biol. *13*, 75–88.

Gaidarov, I., Santini, F., Warren, R.A., and Keen, J.H. (1999). Spatial control of coated-pit dynamics in living cells. Nat. Cell Biol. *1*, 1–7.

Galic, M., Jeong, S., Tsai, F.C., Joubert, L.M., Wu, Y.I., Hahn, K.M., Cui, Y., and Meyer, T. (2012). External push and internal pull forces recruit curvature-sensing N-BAR domain proteins to the plasma membrane. Nat. Cell Biol. *14*, 874–881.

Gustavsson, N., Lao, Y., Maximov, A., Chuang, J.C., Kostromina, E., Repa, J.J., Li, C., Radda, G.K., Südhof, T.C., and Han, W. (2008). Impaired insulin secretion and glucose intolerance in synaptotagmin-7 null mutant mice. Proc. Natl. Acad. Sci. USA *105*, 3992–3997.

Haucke, V., and De Camilli, P. (1999). AP-2 recruitment to synaptotagmin stimulated by tyrosine-based endocytic motifs. Science *285*, 1268–1271.

Haucke, V., Neher, E., and Sigrist, S.J. (2011). Protein scaffolds in the coupling of synaptic exocytosis and endocytosis. Nat. Rev. Neurosci. *12*, 127–138.

He, Z., Fan, J., Kang, L., Lu, J., Xue, Y., Xu, P., Xu, T., and Chen, L. (2008). Ca2+ triggers a novel clathrin-independent but actin-dependent fast endocytosis in pancreatic beta cells. Traffic *9*, 910–923.

Hosoi, N., Holt, M., and Sakaba, T. (2009). Calcium dependence of exo- and endocytotic coupling at a glutamatergic synapse. Neuron *63*, 216–229.

Hua, Y., Sinha, R., Thiel, C.S., Schmidt, R., Hüve, J., Martens, H., Hell, S.W., Egner, A., and Klingauf, J. (2011). A readily retrievable pool of synaptic vesicles. Nat. Neurosci. *14*, 833–839.

Jaqaman, K., Loerke, D., Mettlen, M., Kuwata, H., Grinstein, S., Schmid, S.L., and Danuser, G. (2008). Robust single-particle tracking in live-cell time-lapse sequences. Nat. Methods *5*, 695–702.

Jaqaman, K., Kuwata, H., Touret, N., Collins, R., Trimble, W.S., Danuser, G., and Grinstein, S. (2011). Cytoskeletal control of CD36 diffusion promotes its receptor and signaling function. Cell *146*, 593–606.

Jockusch, W.J., Praefcke, G.J., McMahon, H.T., and Lagnado, L. (2005). Clathrin-dependent and clathrin-independent retrieval of synaptic vesicles in retinal bipolar cells. Neuron *46*, 869–878.

Kadamur, G., and Ross, E.M. (2013). Mammalian phospholipase C. Annu. Rev. Physiol. *75*, 127–154.

Kawasaki, F., Iyer, J., Posey, L.L., Sun, C.E., Mammen, S.E., Yan, H., and Ordway, R.W. (2011). The DISABLED protein functions in CLATHRIN-mediated synaptic vesicle endocytosis and exoendocytic coupling at the active zone. Proc. Natl. Acad. Sci. USA *108*, E222–E229.

Keyel, P.A., Watkins, S.C., and Traub, L.M. (2004). Endocytic adaptor molecules reveal an endosomal population of clathrin by total internal reflection fluorescence microscopy. J. Biol. Chem. *279*, 13190–13204.

Kim, Y.J., Guzman-Hernandez, M.L., and Balla, T. (2011). A highly dynamic ER-derived phosphatidylinositol-synthesizing organelle supplies phosphoinositides to cellular membranes. Dev. Cell *21*, 813–824.

Kononenko, N.L., Puchkov, D., Classen, G.A., Walter, A.M., Pechstein, A., Sawade, L., Kaempf, N., Trimbuch, T., Lorenz, D., Rosenmund, C., et al. (2014). Clathrin/AP-2 mediate synaptic vesicle reformation from endosome-like vacuoles but are not essential for membrane retrieval at central synapses. Neuron *82*, 981–988.

Lansbergen, G., Grigoriev, I., Mimori-Kiyosue, Y., Ohtsuka, T., Higa, S., Kitajima, I., Demmers, J., Galjart, N., Houtsmuller, A.B., Grosveld, F., and Akhmanova, A. (2006). CLASPs attach microtubule plus ends to the cell cortex through a complex with LL5beta. Dev. Cell *11*, 21–32.

Liang, K., Du, W., Zhu, W., Liu, S., Cui, Y., Sun, H., Luo, B., Xue, Y., Yang, L., Chen, L., and Li, F. (2011). Contribution of different mechanisms to pancreatic beta-cell hyper-secretion in non-obese diabetic (NOD) mice during pre-diabetes. J. Biol. Chem. *286*, 39537–39545.

Loerke, D., Mettlen, M., Yarar, D., Jaqaman, K., Jaqaman, H., Danuser, G., and Schmid, S.L. (2009). Cargo and dynamin regulate clathrin-coated pit maturation. PLoS Biol. *7*, e57.

Macia, E., Ehrlich, M., Massol, R., Boucrot, E., Brunner, C., and Kirchhausen, T. (2006). Dynasore, a cell-permeable inhibitor of dynamin. Dev. Cell *10*, 839–850.

Marie, B., Sweeney, S.T., Poskanzer, K.E., Roos, J., Kelly, R.B., and Davis, G.W. (2004). Dap160/intersectin scaffolds the periactive zone to achieve high-fidelity endocytosis and normal synaptic growth. Neuron *43*, 207–219.

McMahon, H.T., and Boucrot, E. (2011). Molecular mechanism and physiological functions of clathrin-mediated endocytosis. Nat. Rev. Mol. Cell Biol. *12*, 517–533.

Merrifield, C.J., Feldman, M.E., Wan, L., and Almers, W. (2002). Imaging actin and dynamin recruitment during invagination of single clathrin-coated pits. Nat. Cell Biol. *4*, 691–698.

Merrifield, C.J., Perrais, D., and Zenisek, D. (2005). Coupling between clathrin-coated-pit invagination, cortactin recruitment, and membrane scission observed in live cells. Cell *121*, 593–606.

Merrins, M.J., and Stuenkel, E.L. (2008). Kinetics of Rab27a-dependent actions on vesicle docking and priming in pancreatic beta-cells. J. Physiol. *586*, 5367–5381.

Montagnac, G., Meas-Yedid, V., Irondelle, M., Castro-Castro, A., Franco, M., Shida, T., Nachury, M.V., Benmerah, A., Olivo-Marin, J.C., and Chavrier, P. (2013). αTAT1 catalyses microtubule acetylation at clathrin-coated pits. Nature *502*, 567–570.

Neher, E. (2010). What is Rate-Limiting during Sustained Synaptic Activity: Vesicle Supply or the Availability of Release Sites. Front. Synaptic Neurosci. *2*, 144.

Ohara-Imaizumi, M., Ohtsuka, T., Matsushima, S., Akimoto, Y., Nishiwaki, C., Nakamichi, Y., Kikuta, T., Nagai, S., Kawakami, H., Watanabe, T., and Nagamatsu, S. (2005). ELKS, a protein structurally related to the active zone-associated protein CAST, is expressed in pancreatic beta cells and functions in insulin exocytosis: interaction of ELKS with exocytotic machinery analyzed by total internal reflection fluorescence microscopy. Mol. Biol. Cell *16*, 3289–3300.

Olivo-Marin, J.C. (2002). Extraction of spots in biological images using multiscale products. Pattern Recognit. *35*, 1989–1996.

Pelassa, I., Zhao, C., Pasche, M., Odermatt, B., and Lagnado, L. (2014). Synaptic vesicles are "primed" for fast clathrin-mediated endocytosis at the ribbon synapse. Front. Mol. Neurosci. *7*, 91.

Roos, J., and Kelly, R.B. (1999). The endocytic machinery in nerve terminals surrounds sites of exocytosis. Curr. Biol. *9*, 1411–1414.

Shen, H., Pirruccello, M., and De Camilli, P. (2012). SnapShot: membrane curvature sensors and generators. Cell *150*, 1300.

Swan, L.E. (2013). Initiation of clathrin-mediated endocytosis: all you need is two? BioEssays *35*, 425–429.

Szent-Gyorgyi, C., Schmidt, B.F., Creeger, Y., Fisher, G.W., Zakel, K.L., Adler, S., Fitzpatrick, J.A., Woolford, C.A., Yan, Q., Vasilev, K.V., et al. (2008). Fluorogen-activating single-chain antibodies for imaging cell surface proteins. Nat. Biotechnol. *26*, 235–240.

Tsuboi, T., McMahon, H.T., and Rutter, G.A. (2004). Mechanisms of dense core vesicle recapture following "kiss and run" ("cavicapture") exocytosis in insulin-secreting cells. J. Biol. Chem. *279*, 47115–47124.

von Kleist, L., Stahlschmidt, W., Bulut, H., Gromova, K., Puchkov, D., Robertson, M.J., MacGregor, K.A., Tomilin, N., Pechstein, A., Chau, N., et al. (2011). Role of the clathrin terminal domain in regulating coated pit dynamics revealed by small molecule inhibition. Cell *146*, 471–484.

Vonesch, C., and Unser, M. (2008). A fast thresholded landweber algorithm for wavelet-regularized multidimensional deconvolution. IEEE Trans. Image Process. *17*, 539–549.

Wahl, S., Katiyar, R., and Schmitz, F. (2013). A local, periactive zone endocytic machinery at photoreceptor synapses in close vicinity to synaptic ribbons. J. Neurosci. *33*, 10278–10300.

Watanabe, S., Rost, B.R., Camacho-Pérez, M., Davis, M.W., Söhl-Kielczynski, B., Rosenmund, C., and Jorgensen, E.M. (2013). Ultrafast endocytosis at mouse hippocampal synapses. Nature *504*, 242–247.

Westrum, L.E., and Gray, E.G. (1986). New observations on the substructure of the active zone of brain synapses and motor endplates. Proc. R. Soc. Lond. B Biol. Sci. *229*, 29–38.

Willig, K.I., Rizzoli, S.O., Westphal, V., Jahn, R., and Hell, S.W. (2006). STED microscopy reveals that synaptotagmin remains clustered after synaptic vesicle exocytosis. Nature *440*, 935–939.

Wu, X.S., McNeil, B.D., Xu, J., Fan, J., Xue, L., Melicoff, E., Adachi, R., Bai, L., and Wu, L.G. (2009). Ca(2+) and calmodulin initiate all forms of endocytosis during depolarization at a nerve terminal. Nat. Neurosci. *12*, 1003–1010.

Yuan, T., Lu, J., Zhang, J., Zhang, Y., and Chen, L. (2015). Spatiotemporal detection and analysis of exocytosis reveal fusion "hotspots" organized by the cytoskeleton in endocrine cells. Biophys. J. *108*, 251–260.

Zhao, Y., Gaidarov, I., and Keen, J.H. (2007). Phosphoinositide 3-kinase C2alpha links clathrin to microtubule-dependent movement. J. Biol. Chem. *282*, 1249–1256.

Zhu, Y., Xu, J., and Heinemann, S.F. (2009). Two pathways of synaptic vesicle retrieval revealed by single-vesicle imaging. Neuron *61*, 397–411.

Zong, W., Huang, X., Zhang, C., Yuan, T., Zhu, L.L., Fan, M., and Chen, L. (2014). Shadowless-illuminated variable-angle TIRF (siva-TIRF) microscopy for the observation of spatial-temporal dynamics in live cells. Biomed. Opt. Express *5*, 1530–1540.